Journal of Sound and Vibration 329 (2010) 3940–3957

Contents lists available at ScienceDirect

Journal of Sound and Vibration

journal homepage: www.elsevier.com/locate/jsvi

Estimation of the far-field directivity of broadband aeroengine fan noise using an in-duct axial microphone array

C.R. Lowis [b], P.F. Joseph [b,*], A.J. Kempton [a]

[a] Rolls Royce plc., PO Box 31, Derby DE24 8BJ, UK
[b] Institute of Sound and Vibration Research, University of Southampton, Southampton SO17 1BJ, UK

ARTICLE INFO

Article history:
Received 27 October 2008
Received in revised form
8 March 2010
Accepted 15 March 2010
Handling Editor: M.P. Cartmell
Available online 1 May 2010

ABSTRACT

This paper presents a measurement technique for estimating the far-field directivity of the sound radiated from a duct using measurements of acoustic pressure made inside the duct. The technique is restricted to broadband, multi-mode sound fields whose directivity patterns are axi-symmetric, and whose modes are mutually uncorrelated. The technique uses a transfer function to relate the output from an in-duct axial beamformer to measurements of the far-field polar directivity. A transfer function for a hollow cylindrical duct with no flow is derived, and investigated in detail. Transfer functions for practical cases concerning aeroengine exhausts are also presented. The transfer function is shown to be insensitive to the mode-amplitude distribution inside the duct, and hence can be used to predict the directivity in practice where the noise source distribution is unknown. The technique is then validated using a no-flow facility, and is shown to be able to predict variations in the far-field directivity pattern and also estimate the far-field sound pressure levels to within 2 dB. It is suggested that the proposed technique will be especially useful for fan rig experiments, where direct measurement of directivity, for example by use of an anechoic chamber, is impossible.

1. Introduction

To test new aeroengine designs model-scale tests are often performed as they provide realistic aerodynamic conditions while at the same time being easy to modify and instrument with sensors. A disadvantage of model-scale tests is that direct measurement of radiated noise is often impractical. Compared to full-scale tests these model-scale tests require a suitable facility, and one which is large enough to both contain the model to be tested and allow measurements to be made in the acoustic far-field. Model-scale tests are often carried out in indoor facilities, where either anechoic facilities do not exist for the measurement of radiated noise or measurement is impossible due to mechanical constraints (venting of gasses for example). Because of this, acoustic measurements are often restricted to locations *within* the bypass duct or inlet duct.

Such model-scale tests therefore require a measurement technique which can estimate the far-field directivity using measurements of acoustic pressure made at the inside wall of the duct. Ideally the technique would allow rapid estimation so that it can be used as part of an iterative design process. This paper presents a technique that fulfils these criteria. The technique is restricted to broadband, multi-mode sound fields whose directivity patterns are axi-symmetric, and whose modes are mutually uncorrelated.

---

[*] Corresponding author.
E-mail addresses: cl@isvr.soton.ac.uk (C.R. Lowis), pfj@isvr.soton.ac.uk (P.F. Joseph), andrew.j.kempton@rolls-royce.com (A.J. Kempton).

0022-460X/$ - see front matter © 2010 Elsevier Ltd. All rights reserved.
doi:10.1016/j.jsv.2010.03.021

Several previous authors have employed in-duct measurement techniques using arrays of microphones to better understand the sources of sound within the duct. In a previous paper [14] the current authors proposed an in-duct beamforming technique to quantify the sources of broadband noise on a rotating, ducted fan using a beamformer whose point of focus followed the rotation of the fan. Sijtsma [5] and Dougherty et al. [11] later implemented experimentally source imaging techniques for noise source quantification and demonstrated the feasibility of the approach. In all cases, however, the focus was on imaging the noise sources and no attempt was made to link these noise sources to the radiated sound from the duct to the far-field.

The only current technique for estimating the radiated directivity patterns from in-duct measurements is to first determine the amplitudes of all the propagating modes in the duct, a process known as *modal decomposition*. The amplitudes of each mode can then be used as the input to a radiation model which describes how each mode propagates to the far-field. Modal decomposition for tonal (rotor–stator interaction) noise is a well-established experimental technique, first applied by Bolleter and Crocker [1] and later extended to ever larger microphone arrays.

Modal analysis of broadband noise is a comparatively less well developed technique. Broadband noise generated by the fan causes all propagating modes to carry energy. As the frequency under consideration increases, the number of modes able to propagate also increases and more microphones are required to accurately decompose the sound field. This involves either using an array with a large number of fixed microphones, as employed by Ganz [2] for example, or by using a smaller number of microphones that can rotate around the duct axis. To use a rotating microphone array, a known phase reference is required, such as that provided by a single stationary microphone. For example, researchers at Boeing [15] have applied modal decomposition to study both fan noise source generation mechanisms, but make no attempt to link the in-duct modal analysis results to the far-field. Enghardt et al. [3,4] have recently proposed techniques to allow the decomposition of broadband sound fields with up to 150 propagating modes.

Predicting the far-field directivity from in-duct measurements using a modal decomposition approach is a very involved process and unsuitable for rapid assessment of directivity patterns due to the complexity of instrumentation and modelling of the radiation patterns of each individual mode. The technique proposed in this paper is designed with rapid predictions in mind, and can be implemented with considerably less complicated microphone arrays than those used in modal decomposition approaches.

In Section 2 the theory of the technique is developed. We start with a definition of a transfer function which describes a one-to-one correspondence between an in-duct mode-ray angle and a corresponding angle in the far-field. The in-duct mode-ray angles are obtained using an axial array of microphones, and, to aid theoretical analysis a simple delay-and-sum beamformer, described in Section 2.3. A transfer function suitable for hollow cylindrical ducts is derived in Section 2.4 using an analytical expression for the radiation pattern. In Section 3 some properties of the transfer function are investigated including a high-frequency asymptotic formulation. The transfer function is extended to a more realistic with-flow case in Section 4. In Section 5 we return to the no-flow formulation and validate its ability to predict the far-field radiation pattern from in-duct measurements using experimental data.

2. Theory

The technique presented here is based on the principle that the angle of the main radiation lobe associated with a particular mode is uniquely and simply related to the in-duct axial propagation angle [6]. In the no-flow case the two angles are identical. The variation of in-duct mean square pressure with axial propagation angle, ϕ, is estimated by an axial beamformer comprising a number of uniformly spaced microphones located at the duct wall. The far-field radiation, $|p_f(\phi_f,\omega)|^2$, at a far-field radiation angle ϕ_f, is then related to the beamformer output, $|b(\phi_b,\omega)|^2$, at an in-duct angle ϕ_b, via a transfer function, $|H(\phi_f,\omega)|^2$,

$$|p_f(\phi_f,\omega)|^2 = |H(\phi_f,\omega)|^2 |b(\phi_b,\omega)|^2 \tag{1}$$

where $|H(\phi_f,\omega)|^2$ is predicted from numerical calculation. It is fundamentally important to recognise that ϕ_b and ϕ_f differ in the general case but are uniquely and closely related. In the hypothetical case of radiation problems where the axial Mach number in the duct and in the far-field are the same (see Section 2.4), $\phi_f = \phi_b$ [6]. In the exhaust duct case presented in Section 4, however, ϕ_f is related to ϕ_b by a simple transformation given by the laws of refraction.

Crucially, the measurement principle is only useful if the transfer function, $|H(\phi_f,\omega)|^2$, does not depend on the mode amplitude distribution (or equivalently the sound source distribution) in the duct since this information is very rarely known *a priori*. This requirement will be investigated later in the paper.

2.1. In-duct sound field in terms of mode-ray angles

At a single frequency, ω, the sound field in a semi-infinite, hard-walled, hollow cylindrical duct with uniform mean-flow is of the form

$$p(\mathbf{x},\omega) = \sum_{mn} A_{mn} \Psi_{mn} \mathrm{e}^{\mathrm{i}(k_{zmn}z+\omega t)} \tag{2}$$

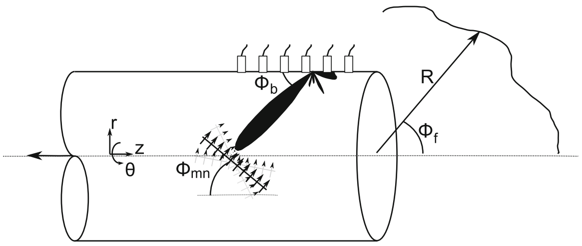

Fig. 1. A schematic of the measurement setup. An axial array of microphones mounted at the duct wall are used to steer a beam at an angle ϕ_b. Individual modes are incident on the array with mode-ray angles ϕ_{mn}. The polar radiation angle is denoted ϕ_f.

where $\mathbf{x}=(r,\theta,z)$ is a location in the duct coordinate system. Fig. 1 is a schematic of the duct, where z is positive along the duct axis towards the duct exit. Ψ_{mn} is the normalised mode of order (m, n), of pressure amplitude A_{mn}, and k_{zmn} is the modal axial wavenumber. In the following, it is convenient to use the notation given by Chapman [7]. Eq. (2) can be re-written as

$$p(\mathbf{x},\omega)=\sum_{mn}A_{mn}\Psi_{mn}\mathrm{e}^{\mathrm{i}(M+\cos\overline{\phi}_{mn})k\overline{\overline{z}}+\mathrm{i}\omega t} \tag{3}$$

where M is the axial flow Mach number, and $k=\omega/c$.

Here the pressure is expressed in Prandtl–Glauert transformed coordinates, with a bar denoting division by the Doppler factor $\beta=\sqrt{(1-M^2)}$, and unless otherwise stated a double bar denoting division by β^2.

In this notation $\overline{\phi}_{mn}$ is the transformed mode ray angle of the mode (m, n) lying in the range $0\le\overline{\phi}\le\pi/2$, defined by

$$\sin\overline{\phi}_{mn}=\frac{\sigma_{mn}}{k\overline{a}} \tag{4}$$

where σ_{mn} is the eigenvalue of the (m, n)th mode. The axial wavenumber is given by

$$k_{zmn}=(M+\cos\overline{\phi}_{mn})k/\beta^2 \tag{5}$$

Note that $\overline{\phi}_{mn}$ is related to the actual mode-ray angle ϕ_{mn}, that is the angle at which the mode propagates relative to the duct axis, by

$$\sin\phi_{mn}=\frac{\sin\overline{\phi}_{mn}}{(1-M^2\cos^2\overline{\phi}_{mn})^{1/2}} \tag{6}$$

2.2. Far-field radiation for flow everywhere the same

The transfer function $|H(\phi_f,\omega)|^2$, defined in Eq. (1), will initially be predicted using the far-field modal directivity pattern for a flanged, semi-infinite duct. The expression, expressed here in Chapman's [7] notation, for far-field radiation in which the *flow speed is the same everywhere* is

$$p_f(\overline{\phi}_f,\omega)=\sum_{mn}A_{mn}\Lambda_{mn}a^2\cos\overline{\phi}_{mn}\frac{(-\mathrm{i})^{m+1}k}{2\beta^2\overline{\overline{R}}}\mathrm{e}^{-\mathrm{i}m\theta+\mathrm{i}Mk\overline{\overline{z}}+\mathrm{i}k\overline{\overline{R}}}\mathrm{e}^{\mathrm{i}\omega t}d(\overline{\phi}_f,\overline{\phi}_{mn}) \tag{7}$$

where $\Lambda_{mn}=[1-m^2/\sigma^2_{mn}]^{-1}$ is the mode normalisation constant and $\overline{\overline{R}}=(\overline{\overline{z}}^2+\overline{r})^{1/2}$ (see Fig. 1) is the distance from the centre of the open duct face to the far-field measurement location. In Eq. (7),

$$d(\overline{\phi}_f,\overline{\phi}_{mn})=\frac{-2(\sin\overline{\phi}_f)J'_m(k\overline{a}\sin\overline{\phi}_f)\mathrm{e}^{-\mathrm{i}k\overline{\overline{d}}(\cos\overline{\phi}_f-\cos\overline{\phi}_{mn})}}{k\overline{a}(1-m^2/\sigma^2_{mn})J_m(\sigma_{mn})(\sin^2\overline{\phi}_f-\sin^2\overline{\phi}_{mn})} \tag{8}$$

are the non-dimensional modal directivity functions given by Chapman [7] such that $d(\overline{\phi}_f,\overline{\phi}_{mn})=1$ for $\overline{\phi}_f=\overline{\phi}_{mn}$. Rice [6] shows that the angle $\overline{\phi}_{mn}$ at which peak radiation occurs corresponds to the group velocity angle, i.e., the angle at which energy is transmitted along the duct.

In Section 4 we use a more realistic unflanged duct model for the far-field radiation to predict $|H(\phi_f,\omega)|^2$ that takes into account, for example, shear layers in the flow due to a by-pass duct.

2.3. Beamformer formulation

The axial beamformer, required by the measurement technique, comprises N equally spaced microphones arranged along the duct wall, $r_l=a$, at a fixed circumferential position, such that $\overline{\overline{z}}_l=l\Delta z/\beta^2$ (l=0,1,…,$N-1$), where Δz is the spacing between adjacent microphones at the duct wall. The beamformer response is formulated by multiplying the complex pressures at each microphone by a complex weighting coefficient, w_l^*, and summing such that the signals at each microphone due to a single mode propagating at the beam-steer angle, $\overline{\phi}_b$, add in phase

$$b(\overline{\phi}_b,\omega)=\frac{1}{N}\sum_{l=0}^{N-1}p(\overline{\overline{z}}_l,\omega)w_l^*(\overline{\phi}_b) \tag{9}$$

where

$$w_l(\overline{\phi}_b)=\mathrm{e}^{+\mathrm{i}(M+\cos\overline{\phi}_b)k\overline{\overline{z}}_l} \tag{10}$$

Substituting Eq. (3) for the pressure into (9) gives

$$b(\overline{\phi}_b,\omega)=\sum_{mn}A_{mn}\Psi_{mn}T(\overline{\phi}_{mn},\overline{\phi}_b) \tag{11}$$

where the time dependence has been dropped and $T(\overline{\phi}_{mn},\overline{\phi}_b)$ is the beamformer response function,

$$T(\overline{\phi}_{mn},\overline{\phi}_b)=\frac{1}{N}\sum_{l=0}^{N-1}\mathrm{e}^{\mathrm{i}(\cos\overline{\phi}_{mn}-\cos\overline{\phi}_b)k\overline{\overline{z}}_l} \tag{12}$$

Note that because the phase delay in Eq. (10) is chosen to correspond to the modal phase velocity (see Chapman [7]) the dependence on Mach number in the beamformer response cancels and the maximum output of the beamformer due to a particular mode occurs when the group velocity angle equals the beamformer angle, that is $T(\overline{\phi}_{mn},\overline{\phi}_b)=1$ for $\overline{\phi}_b=\overline{\phi}_{mn}$. Thus, there is exact correspondence between the beamformer angle ϕ_b and the radiation angle.

For broadband noise, the modes may be assumed to be uncorrelated and the mod-square beamformer output can be written as

$$|b(\overline{\phi}_b,\omega)|^2=\sum_{mn}|p_w(\overline{\phi}_{mn},\omega)|^2|T(\overline{\phi}_{mn},\overline{\phi}_b)|^2 \tag{13}$$

where $|p_w(\phi_{mn},\omega)|^2$ is the squared pressure at the duct wall due to the $(m,\ n)$th mode, given by, for the case of a hollow cylindrical duct,

$$|p_w(\overline{\phi}_{mn},\omega)|^2=\frac{|A_{mn}|^2}{\Lambda_{mn}} \tag{14}$$

The squared pressure at the duct wall is the incoherent sum of the modal components

$$|p_w(\omega)|^2=\sum_{mn}|p_w(\overline{\phi}_{mn},\omega)|^2 \tag{15}$$

2.4. In-duct to far-field transfer function for flow everywhere the same

Combining Eqs. (1), (7), (13) and (14) the in-duct to far-field transfer function for a flanged duct radiation problem in which the flow speed is everywhere the same is

$$4\left(\frac{\overline{R}}{\overline{a}}\right)^2|H(\overline{\phi}_f,\omega)|^2=\frac{(k\overline{a})^2\sum_{mn}|A(\overline{\phi}_{mn})|^2\Lambda_{mn}^2|d(\overline{\phi}_f,\overline{\phi}_{mn})|^2\cos^2\overline{\phi}_{mn}}{\sum_{mn}|A(\overline{\phi}_{mn})|^2\left(1-\frac{m^2}{\sigma_{mn}^2}\right)^{-1}|T(\overline{\phi}_{mn},\overline{\phi}_b)|^2} \tag{16}$$

and the steer-angle of the beamformer matches the radiation angle, $\overline{\phi}_b=\overline{\phi}$.

An essential condition for the measurement technique to be valid is that the transfer function, $|H(\overline{\phi}_f,\omega)|^2$, must be independent of mode amplitude distribution. In Sections 3.3 and 4 we demonstrate that this condition is valid to within 1 or 2 dB over a range of extreme mode amplitude distributions for both no-flow ducts, and a typical exhaust duct configuration.

2.5. Mode amplitude distribution models

The simulations presented later in the paper are based on idealised mode amplitude distribution models. Joseph et al. [8] present various models for $|A(\overline{\phi}_{mn})|^2$. The practical validity of these models for aeroengine applications has also been studied by Castres et al. [19]. The first model used here assumes *equal amplitude per mode*, that is,

$$|A(\overline{\phi}_{mn})^{\mathrm{ea}}|^2=\mathcal{A}^2 \tag{17}$$

where $\mathcal{A}$ is the modulus of the modal pressure, assumed constant for all cut-on modes.

The second model assumes *equal energy per mode* namely that all cut-on modes carry equal sound power

$$|A(\overline{\phi}_{mn})^{\rm ee}|^2 = \frac{2\rho c}{\pi a^2}\varpi\frac{1}{(\cos\overline{\phi}_{mn})}\frac{(1-M\cos\overline{\phi}_{mn})^2}{\beta^2} \tag{18}$$

where ϖ is the sound power carried by a single mode above cut-off.

Another family of mode distribution models is obtained by assuming that the source plane can be modelled as a distribution of incoherent point-sources of arbitrary temporal and spatial order, v and μ respectively,

$$|A(\overline{\phi}_{mn})^{\mu,v}|^2 \propto \frac{1}{\cos^2\overline{\phi}_{mn}}\left(\frac{M-\cos\overline{\phi}_{mn}}{\beta^2}\right)^{2\mu}\left(\frac{1-M\cos\overline{\phi}_{mn}}{\beta^2}\right)^{2v} \tag{19}$$

where special cases are a distribution of volume velocity (monopole) sources, in which case, $(\mu,v)=(0,2)$, and a distribution of dipole sources $(\mu,v)=(1,0)$.

3. No-flow results

In this section we will present simulation results to illustrate the use of the technique for determining the radiation directivity from a hollow cylindrical duct with no-flow, that is, quiescent conditions. Although this situation is unrepresentative of aeroengine situations the comparative simplicity of the problem more easily allows physical interpretation, and as presented elsewhere [10,16], experimental validation of the results. In all cases in this section $M=0$ and hence we drop the overbar on ϕ_b and ϕ_f to make this explicit.

3.1. Beamformer response due to the presence of a single mode

Fig. 2 shows the beamformer output as a function of steering angle due to a single mode of unit amplitude at the duct wall, $|p_w(\phi_{mn},\omega)|^2=1$, for the (0, 0), (10, 0) and (17, 0) modes for $M=0$ at $ka=20$. The array has 11 microphones separated by a distance $\Delta z=\lambda/2$ to give a total array length of 5λ. The maximum output of the beamformer in each case can be seen to correspond to the mode ray angles, which are $\phi_{mn}=0^\circ$, $\phi_{mn}=36^\circ$ and $\phi_{mn}=73^\circ$ respectively. Note also that the beamwidth increases as the beam is steered towards $\phi_b=0$ (end-fire).

We now investigate the beamformer output for a multi-mode sound field for the idealised mode amplitude distribution models given in Section 2.5.

3.2. Beamformer response to multi-mode sound field

A expression for the variation of beamwidth with steering angle can be derived by noting that the beamformer directivity function of Eq. (12), for a fixed microphone spacing Δz, can be written as

$$|T(\phi_{mn},\phi_b)| = \frac{\sin\left[\frac{N}{2}k\Delta z(\cos\phi_{mn}-\cos\phi_b)\right]}{N\sin\left[\frac{1}{2}k\Delta z(\cos\phi_{mn}-\cos\phi_b)\right]} \tag{20}$$

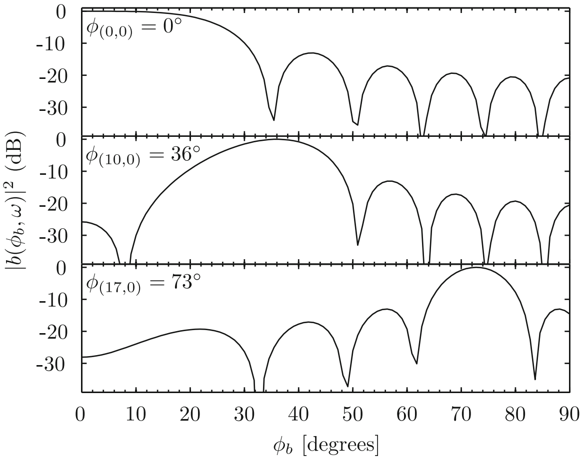

Fig. 2. Beamformer output as a function of steering angle calculated for excitation by the (0, 0) (top), (10, 0) (middle) and (17, 0) (bottom) mode at $ka=20$. As the mode order increases the modes become progressively less well cut-on and the mode-ray angle increases (Eq. (4)).

We define the array beamwidth, ϕ_{BW}, as one-half of the angle separation between the first zero crossings, $|T(\phi_{mn}, \pm\phi_0)| = 0$, either side of the mainlobe peak ϕ_{mn}. The zero crossings occur when the numerator of Eq. (20) is zero. For simplicity we assume the beampattern is symmetrical about its peak. The beamwidth for a beam steered at $\phi_b = \phi_{mn}$ is given by

$$\phi_{\mathrm{BW}} = \frac{1}{2}[2(\phi_0 - \phi_{mn})] = \cos^{-1}\left[\frac{2\pi}{Nk\Delta z} - \cos\phi_{mn}\right] - \phi_{mn} \tag{21}$$

Eq. (21) shows that the beamwidth decreases as the length of the array $L_z = (N-1)\Delta z$ increases, and increases for ϕ_{mn} close to zero. However as ϕ_b tends to 0 the mainlobe of the beam approaches the end-fire angles, progressively more of the mainlobe is "lost" to angles outside of the duct. The area under the mainlobe decreases, and in the multi-mode case, this will cause a reduction in the beamformer output. To compensate for this, for angles from $\phi_b = 0$ to $\phi_b = \phi_{\mathrm{BW}}$ the following correction is applied:

$$b(\phi_b) = \begin{cases} b(\phi_b) + b(\phi_{\mathrm{BW}} - \phi_b) & \text{for } \phi_b \le \phi_{\mathrm{BW}} \\ b(\phi_b) & \text{for } \phi_b > \phi_{\mathrm{BW}} \end{cases} \tag{22}$$

this can be interpreted as adding to the beamformer output in the correction region that which would be measured "outside" of the duct.

Fig. 3 is a plot of the corrected beamform output as a function of steering angle for the three mode models presented in Section 2.5. The array parameters are $N=11$, $\Delta z = \lambda/2$, the frequency is $ka=20$. To allow the comparison between the different mode models the beamformer output is normalised by $\int_0^{\pi/2} |b(\phi_b,\omega)|^2 \sin\phi_b \, d\phi_b$. Note that in Fig. 3 the response due to an equal energy per mode sound field is very nearly independent of beam-steer angle for angles below approximately 70°.

3.3. Transfer function $|H(\phi_f,\omega)|^2$ for the no-flow cylindrical duct

Fig. 4 is a plot of $|H(\phi_f,\omega)|^2$, calculated from Eq. (16), as a function of steering angle calculated for three different mode amplitude distributions (equal amplitude, equal energy and volume velocity) at $ka=20$. The in-duct array has a length $L_z = 5\lambda$ with $\Delta z = \lambda/2$, and no flow is assumed. For normalisation purposes, $|H(\phi_f,\omega)|^2$ is multiplied by $(8/N)(R/a)^2$ as explained in Section 3.4.

Fig. 4 shows that for angles below approximately 70° the transfer function $|H(\phi_f,\omega)|^2$ is largely independent, to within 2 dB, of the chosen mode amplitude distributions, even though these distributions differ significantly. The bold dash-dot curve in Fig. 4 is a high-*ka* approximation to Eq. (16) which shall be derived in the next section.

The largest deviation from the high-*ka* approximation is observed for the equal amplitude source model at higher ϕ. This is due to the behaviour of $|A_{mn}|^2$ for near cut-off modes approaching infinity as $\phi_b \to \pi/2$ in Eq. (19). This causes the beamformer response to be dominated by individual modes close to cut-on.

3.4. A high-ka approximation for the in-duct to far-field transfer function $|H(\phi_f,\omega)|^2$ for no flow

The in-duct to far-field transfer function in Eq. (16) can be predicted from knowledge of the array length, number of microphones and their axial spacing, together with an appropriate radiation model. However, in this section we derive a simple analytic expression for $|H(\phi_f,\omega)|^2$ that is valid in the high-*ka* limit and for no flow.

In the previous section we demonstrated that while the beamformer output depends on the mode amplitude distribution the transfer function $|H(\phi_f,\omega)|^2$ is insensitive to it. In order to derive a closed form approximation for

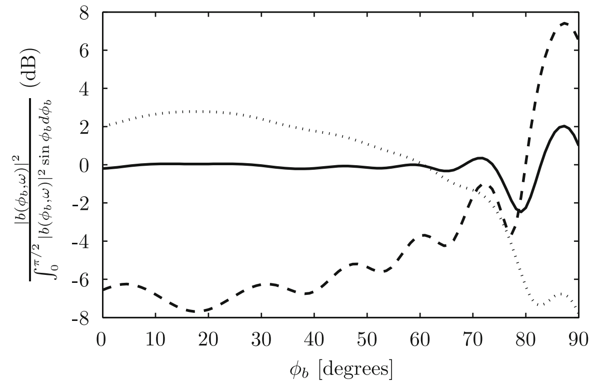

Fig. 3. Beamformer output as a function of steering angle for $ka=20$ and $M=0$, by an equal energy per mode sound field (solid), an equal modal amplitude sound field (dotted) and a distribution of volume velocity sources (dashed).

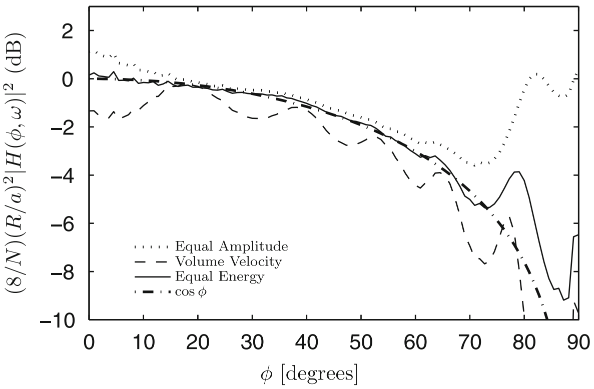

Fig. 4. A plot of the transfer function $|H(\phi_f,\omega)|^2$ as a function of steering angle, calculated for three different mode amplitude distributions at $ka=20$ and $M=0$.

$|H(\phi_f,\omega)|^2$ that is valid in the limit of high frequency, we can therefore chose a particular mode amplitude distribution. If we assume the sound field in the duct has equal energy per mode and that the flow speed can be neglected, there exists a simple expression for the high-*ka* far-field radiation pattern. This result can then be used to derive a high-*ka* approximation for the beamformer output in an equal energy per mode sound field by showing first that this sound field is equivalent to a semi-isotropic noise field, for which a simple expression for $|b(\phi_b,\omega)|^2$ exists. Combining the two results gives a high-*ka* approximation to $|H(\phi_f,\omega)|^2$.

Following Joseph and Morfey [17] the far-field radiation from an unflanged duct containing an equal energy per mode sound field in the limit as $ka\to\infty$ is

$$|p_f(\phi_f,\omega)|^2 = \frac{2\rho c W}{\pi R^2}\cos\phi_f \quad (ka\to\infty) \tag{23}$$

where R is the observer distance from the centre of the duct face and W is the total radiated sound power.

We now consider the in-duct beamformer output for an equal-energy-per-mode sound field. We will make use of a concept widely used in SONAR theory. The *array gain* of a phased array quantifies its level of noise rejection. It is defined as the ratio of the noise power of an omnidirectional sensor to the noise power output detected by the beamformer at a particular beam-steer angle. Applied to the present problem it may be defined as

$$\mathrm{AG}(\phi_b) = \frac{|p_w(\omega)|^2}{|b(\phi_b,\omega)|^2} = \frac{\sum_{mn}|p_w(\phi_{mn},\omega)|^2}{\sum_{mn}|p_w(\phi_{mn},\omega)|^2|T(\phi_{mn},\phi_b)|^2} \tag{24}$$

Noting that the mean-square pressure at the wall of the duct is approximately twice that averaged over the duct cross-section [8], and replacing the summation over $(m,\ n)$ by an integral over ϕ_b, a high frequency approximation for the squared pressure at the duct wall is of the form

$$\sum_{mn}|p_w(\phi_{mn},\omega)|^2 \to 2\mathcal{N}(ka)\int_0^{\pi/2}|A(\phi_b)^{\mathrm{ee}}|^2 n(\phi_b)\,d\phi_b \tag{25}$$

as $(ka\to\infty)$, where $\mathcal{N}(ka)$ is the total number of propagating modes at a frequency ka and $n(\phi_b)$ is the modal density function, which specifies the number of modes, $\mathcal{N}(\phi_b)$ per unit in-duct propagation angle $\delta\phi_b$,

$$n(\phi_b) = \frac{1}{\mathcal{N}(ka)}\frac{\mathcal{N}(\phi_b)-\mathcal{N}(\phi_b-\delta\phi_b)}{\delta\phi_b} \tag{26}$$

It may be shown using the modal density function due to Rice [20] expressed in terms of the cut-off ratio, for $M=0$, that $n(\phi_b)=2\cos\phi_b\sin\phi_b$. Noting that at high ka, $\mathcal{N}(ka)\approx(\frac{1}{2}ka)^2$ [20], inserting Eq. (18) into (25) leads to a simple expression for the squared pressure at the duct wall of the form

$$\sum_{mn}|p_w(\phi_{mn},\omega)|^2 \to 2(ka)^2\frac{\rho c\varpi}{\mathcal{S}} \quad (ka\to\infty) \tag{27}$$

where $\mathcal{S}$ is the duct cross-sectional area πa^2.

In Appendix A we demonstrate that an equal energy per mode sound field, in the high-*ka* limit, tends to a semi-isotropic sound field, in which the mean square pressure arriving per unit solid angle over a hemisphere is constant. The array gain for a line array of N sensors separated by a distance Δz, and steered at an angle ϕ_b in a semi-isotropic noise field is given by [21]

$$\mathrm{AG}(\phi_b) = \frac{N^2}{2N+4\sum_{l=1}^{N}(N-l)\cos(2\pi l\Delta z\cos\phi_b/\lambda)\mathrm{sinc}(2l\Delta z/\lambda)} \tag{28}$$

Here we have assumed that the array gain for a line array in a semi-isotropic noise field is half that in a fully isotropic noise field, since the noise due to a single sensor in the former case is half that in the latter, while the beamformed noise is largely the same in both cases. Substituting Eq. (27) into Eq. (24) gives

$$|b(\phi_b,\omega)|^2 = \frac{2(ka)^2}{\mathrm{AG}(\phi_b)}\frac{\rho c\varpi}{\mathcal{S}} \quad (ka\to\infty) \tag{29}$$

Finally, combining Eqs. (29) and (23) and noting that for the case of equal energy per mode $W/\varpi = \mathcal{N}(ka)\to(\frac{1}{2}ka)^2$ as $ka\to\infty$,

$$\left(\frac{2R}{a}\right)^2 \frac{|H(\phi_f,\omega)|^2}{\mathrm{AG}(\phi_b)} \to \cos\phi_f \quad (ka\to\infty) \tag{30}$$

Note that for $\Delta z = \lambda/2$ in Eq. (28) the array gain $\mathrm{AG}(\phi) = \frac{1}{2}N$. In this case Eq. (29) simplifies to

$$|b(\phi_b,\omega)|^2 = \frac{4(ka)^2\rho c\varpi}{N\mathcal{S}} \quad (\Delta z = \lambda/2, \quad ka\to\infty) \tag{31}$$

and therefore,

$$\frac{8}{N}\left(\frac{R}{a}\right)^2 |H(\phi_f,\omega)|^2 \to \cos\phi_f \quad (ka\to\infty) \tag{32}$$

where the reader is reminded that $\phi_f = \phi_b$ in this special case of no flow.

Eq. (32) is plotted in Fig. 4, for N=11 and ka=20, and is seen to be in very close agreement with the exact calculation of $|H(\phi_f,\omega)|^2$ from Eq. (16).

3.5. *Comparison of in-duct and theoretical array gain*

Fig. 5 is a comparison of the theoretical array gain for a line array in a semi-isotropic noise field as predicted by Eq. (28) with the expression for a linear array at the duct wall versus frequency for equal energy per mode as predicted by Eq. (24) for an array of 11 sensors. The frequency axis is normalised to the reference frequency ka_0=20 at which $\Delta z = \lambda/2$. In general, reasonable agreement between the ideal (dashed) curve and the in-duct array gain (solid curve) is observed. As frequency increases the array gain tends to a value of $10\log_{10}(N/2)$, except at $\phi_b = 0$ where the exact array gain is around 1 dB less than the ideal array gain, attributable to the end-fire effect described in Section 3.2. For a beam-steer angle of $\phi_b = 90^\circ$ (broadside), the agreement with the ideal array gain is less close. The exact array gain fluctuates significantly. This can be attributed to the fact that only a few modes have mode-ray angles close to 90° and hence the semi-isotropic assumption is less valid for high angles close to broadside. At 45°, where the mode density is the highest, and the sound field is at its "most isotropic", the agreement is closest.

3.6. *Estimation of mode amplitude distribution from beamformer output*

In this section we investigate the use of the in-duct beamformer for estimating the distribution of mode amplitude with propagation angle ϕ. In Eq. (13) the beamformer output is formulated as a convolution of the pressure measured at the duct wall, $|p_w(\phi_{mn},\omega)|^2$, with the beamformer response function. At high-ka the squared pressure at the duct wall is approximately twice that averaged over the duct cross section. Assuming that the variation of $|A(\phi_{mn})|^2$ over the

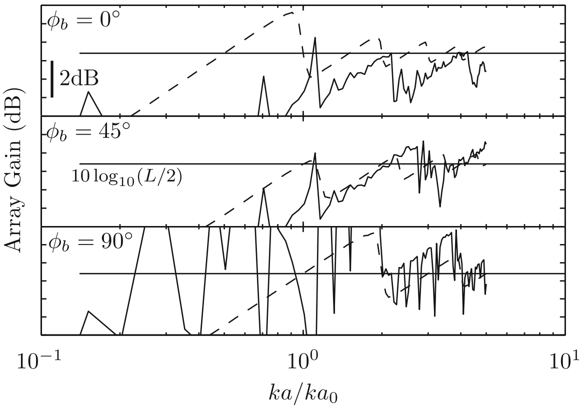

Fig. 5. A comparison of array gain for a line array in a semi-isotropic noise field as predicted by Eq. (28) with that of a linear array at the duct wall as predicted by Eq. (24). Calculated for an array of 11 sensors as a function of frequency, where ka_0=20 is the frequency at which $\Delta z = \lambda/2$. From top to bottom the beam-steer angle is $\phi_b = 0^\circ$ (endfire), $\phi_b = 45^\circ$ and $\phi_b = 90^\circ$ (broadside).

beamwidth is small, and that the beamformer response is negligible at angles away from the beamwidth, the variation of $|A(\phi_{mn})|^2$ can be removed from the integral in Eq. (25), and the integral can be confined to the beamwidth of the array,

$$|b(\phi_b,\omega)|^2 \approx 2\mathcal{N}(ka)|A(\phi_b)|^2 \int_{\phi_b-\Delta\phi_b}^{\phi_b+\Delta\phi_b} n(\phi_b)\,d\phi_b \tag{33}$$

where the integral over ϕ_b specifies the number of modes in the beamwidth $2\Delta\phi_b$ divided by the total number of modes. Noting that for a cylindrical duct, $n(\phi_b)=\sin 2\phi_b$ [20], and performing the integration, the squared mode amplitude averaged over a beamwidth may be estimated as

$$|A(\phi_b)|^2 \approx \frac{|b(\phi_b,\omega)|^2}{\mathcal{N}(ka)[2\sin 2\phi_b \sin 2\Delta\phi_b]} \tag{34}$$

Angles $\phi_b-\Delta\phi_b$ less than zero correspond to the situation where part of the mainlobe is outside of the duct, and ϕ_b is taken to be zero. The variation of mode amplitude with ϕ_b calculated by the approximation in Eq. (34) is plotted in Fig. 6a for an equal-energy-per-mode sound field with unit power per mode at ka=20. Also shown is the exact distribution (crosses). The beamformer has 21 equally spaced sensors $\Delta z=\lambda/2$ apart. In Fig. 6b the exact mode amplitude distribution is generated by multiplying the equal-energy-per-mode distribution from plot (a) by $10^{\alpha \sin\beta\phi_b}$ where $\alpha=0.15$ and $\beta=10$. Fig. 6c is the corresponding result when $|A(\phi_b)|$ varies on a scale roughly equal to a beamwidth, that is $\alpha=0.15$ and $\beta=30$. The beamwidth in the simulations varies from approximately 20° at $\phi_b=0$ to approximately 6° at $\phi_b=90$.

In Fig. 6 the error between the actual and estimated mode amplitude distribution is smallest in the range of propagation angles between 20° and 70°. At low beam-steer angles the difference between the actual and estimated mode amplitudes is larger although the error is still less than 3 dB at 0°. This error can be attributed to the "end-fire" effect mentioned above, where the mainlobe of the beam lays partly outside the duct. With the mode amplitude distribution that varies on a scale larger than a beamwidth, Fig. 6b, the measurement obtained using the in-duct beamformer captures the main variation of the distribution especially in the angle range 20–70°. When the variation of mode amplitude is on a scale equal to or smaller than the beamwidth, the beamformer is not able to follow all of the details of the variation, especially at beam-steer angles close to endfire. However, an "average" modal distribution is captured, and increasing the length of the array (thereby reducing the beamwidth) would improve resolution of the mode amplitude variation. The estimation may also be improved by employing more sophisticated beamforming approaches, such as the deconvolution method proposed by Brooks [9]. Another interesting avenue for future research is whether the estimated distribution of mode amplitudes as a function of mode-ray angle could be used directly as the input to a radiation model.

3.7. Sound power estimation using the in-duct beamformer

In this section we investigate the use of the beamformer measurement for the determination of radiated sound power. The radiated sound power, for axi-symmetric radiation, can be inferred from measurements of the far-field intensity by integrating over a surface enclosing the duct exit, written as

$$W(\omega)=\frac{2\pi R^2}{\rho c}\int_0^{\pi/2} |p_f(\phi_f,\omega)|^2 \sin\phi_f\,d\phi_f \tag{35}$$

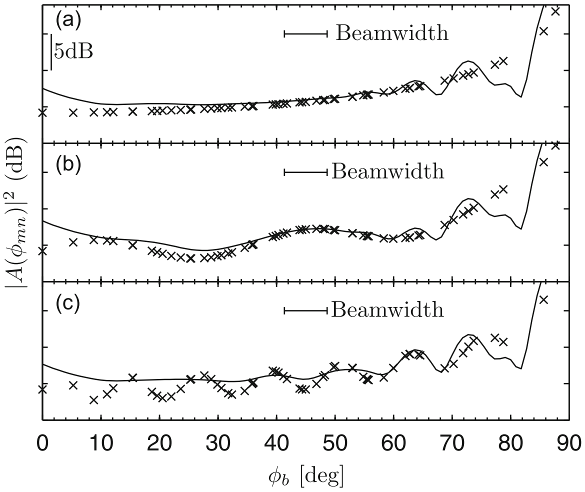

Fig. 6. A comparison of the true mode amplitudes (crosses) and the approximation calculated from the beamformer response function using Eq. (34) at ka=20 with an array of 21 sensors spaced $\Delta z=\lambda/2$. Plot (a) is for an equal energy per mode sound field, plot (b) has $|A(\phi_{mn})|^2$ varying on a scale larger than a beamwidth and plot (c) has $|A(\phi_{mn})|^2$ varying on a scale approximately equal to a beamwidth.

The far-field radiated pressure, $|p_f(\phi_f,\omega)|^2$, can be estimated from the transfer function, $|H(\phi_f,\omega)|^2$, derived earlier. Substituting Eq. (1) and the approximation to $|H(\phi_f,\omega)|^2$ from Eq. (32) into Eq. (35) gives an expression for the radiated sound power in terms of the in-duct beamformer measurements in the high-*ka* limit,

$$W(\omega)=\frac{\mathcal{S}N}{8\rho c}\int_0^{\pi/2}|b(\phi_b,\omega)|^2\sin 2\phi_b\,d\phi_b \tag{36}$$

In Eq. (36) we assume that there are no reflections from the open end of the duct, and that the energy propagating in the mode-ray angles from 0 to $\pi/2$ is radiated to the far-field. In the case where reflections can be considered important Eq. (36) can be modified by subtracting the reflected sound power from the power flowing towards the open end,

$$W(\omega)=W_{\text{incident}}-W_{\text{reflected}}=\frac{\mathcal{S}N}{8\rho c}\left(\int_0^{\pi/2}|b(\phi_b,\omega)|^2\sin 2\phi_b\,d\phi_b-\int_{\pi/2}^{\pi}|b(\phi_b,\omega)|^2\sin 2\phi_b\,d\phi_b\right) \tag{37}$$

Fig. 7 is a plot of the beamformer output between 0° and 180° for an equal energy per mode sound field using an array of N sensors separated axially by $\lambda/2$, with N chosen such that the array length L_z varies from 2λ to 50λ. The frequency is ka=20 and reflections from the open end are assumed to be completely absent. The beamformer output in the range of beam-steer angles from 90° to 180° is due to the presence of side-lobes pointing upstream. The output in this range of angles is approximately 10 dB lower than the maximum output for the shortest array, increasing to 25 dB for the longest array. Thus, the performance of the array in rejecting noise propagating from the opposite direction from the direction of the main sources (caused by, for example, reflection or from the presence of other sources such as valves) appears, at least in this example, to improve as $\approx\log_{10}N$. This implies that Eq. (37) can be used to separate incident and reflected sound power if the difference between them is less than these rejection values. Increased rejection is achieved using longer arrays. It may be possible to improve on the rejection by choosing beamformer weights (known as "shading") that increase side-lobe rejection, at the expense of increased main-lobe width. This is beyond the scope of the current work, but in-depth coverage is available, for example, by Burdic [21].

An interesting analytical result can be derived in the case where the microphone separation distance is $\Delta z=\lambda/2$, and the noise field is perfectly isotropic. At this separation distance the pressure at the wall at each of the individual sensors is uncorrelated (see for example Burdic [21]) and the beamformer output is simply,

$$|b(\phi_b,\omega)|^2=\frac{1}{N^2}[|p_w(\omega)|^2N] \tag{38}$$

and is therefore independent of beamformer angle.

Substituting Eq. (38) into Eq. (36) gives a simple relationship between the radiated sound power and the squared pressure at the wall for the idealised case of equal energy per mode,

$$W(\omega)=\frac{\mathcal{S}|p_w(\omega)|^2}{4\rho c} \tag{39}$$

This result is identical to that obtained by Joseph et al. [8] for the determination of radiated sound power from measurements of pressure at the duct wall for an equal energy per mode sound field.

Having established some basic physical principles using a simplified no-flow model we now consider application of the technique to a simulated exhaust duct, where there are two flow streams.

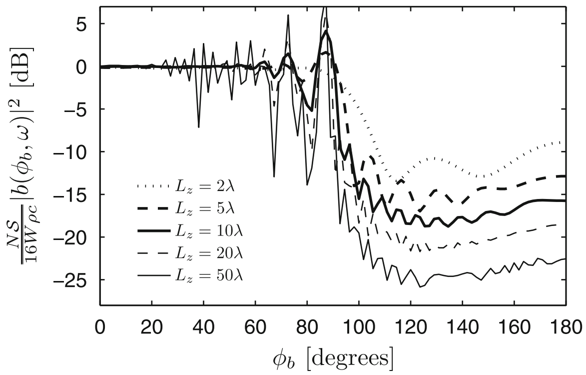

Fig. 7. Beamformer output as a function of beam-steer angle ϕ_b for an equal energy per mode sound field using arrays of varying length L_z with sensors separated axially by $\lambda/2$ at ka=20.

4. Estimation of sound-radiation from aeroengine exhausts

In this section we consider the use of the in-duct beamformer technique to predict the sound radiation from an aeroengine exhaust. The exhaust is modelled as a hard-walled annular duct with a hub-to-tip ratio (the ratio of the inner radius, R_1, to the outer radius, R_0) of 0.8. The calculation of the in-duct beamformer output proceeds as before for the cylindrical duct with the substitution of annular mode shape functions Ψ in Eq. (2).

Fig. 8 is a schematic of the duct geometry used to simulate the exhaust radiation problem. There are two flow streams, one is the flow from the jet with a Mach number M_2, the other is the surrounding mean-flow flight stream which has a Mach number of M_1.

For the purpose of this simulation we predict the far-field radiation pattern for different source models using Gabard and Astley's [22] solution for the radiation from an unflanged annular duct with an infinite centre body. This model, an extension of Munt's solution [23], provides an exact solution for the sound field radiated by a single duct mode from an unflanged annular duct with a hard centre-body. Diffraction through the semi-infinite vortex sheet which separates the annular jet stream from the ambient external flow is included. The model has been successfully validated against no-flow experimental and numerical data by Sugimoto and Astley [24].

An additional complication is introduced by the presence of two flow streams. As a ray leaves the duct it travels through the shear layer separating the two flow streams and is refracted. The relationship between the in-duct angle ϕ_b and the far-field angle ϕ_f can be estimated using Snell's law

$$\phi_f = \cos^{-1}\frac{\cos\phi_b}{1+(M_2-M_1)\cos\phi_b} \tag{40}$$

When $M_2 > M_1$, as is inevitably the case with aeroengine exhausts, the range of far-field angles is smaller than the range of in-duct angles. In Eq. (40), we define the "critical angle" ϕ_c as the value of ϕ_f when $\phi_b = 0$. The range of far-field angles below the critical angle is known as the "cone of silence". Sound is only able to enter the cone of silence by diffraction of the rays [25]. Eq. (40) gives a one-to-one relationship between in-duct and far-field angles, which we use to relate beamformer angle to radiation angle in Eq. (1). This means that the transfer function approach can only be used to predict radiation outside of the cone of silence.

Figs. 9a, b, and c are plots of the beamformer output, far-field directivity and transfer function respectively for an annular duct at ka=20. An array of 11 microphones spaced $\Delta z = \lambda/2$ apart was used for the in-duct beamformer. The figure shows curves for equal amplitude, equal energy and volume velocity mode amplitude distributions. The flow-speeds used for the calculation are M_1=0.4 and M_2=0.6.

Fig. 9a is a plot of beamformer output as a function of transformed in-duct angle $\overline{\phi}_b$ for each of the mode models. The beamformer output is largely independent of the chosen mode amplitude distribution below 50°. At higher angles the curves begin to diverge as the prediction becomes sensitive to the fewer propagating modes with high mode-ray angles as in Fig. 3 for the no-flow case.

Fig. 9b is a plot of the far-field radiation pattern predicted using the Gabard–Astley radiation model for each of the mode amplitude distributions as a function of the transformed angle $\overline{\phi}_f$. The radiation pattern is largely independent of the chosen mode amplitude model. Note also that the Gabard–Astley model predicts radiation inside the cone of silence, at angles below the critical angle 33.5° which cannot be deduced from the in-duct beamformer.

Fig. 9c plots $|p_f(\phi_f,\omega)|^2/|b(\phi_b,\omega)|^2$, corresponding to the transfer function obtained by dividing the radiation at an angle ϕ_f by the beamformer output at an angle ϕ_b where the two angles are related by Eq. (40). The transfer function is undefined for angles below the critical angle since Eq. (40) is undefined for $\phi_f < \phi_c$ and there is no longer a one-to-one correspondence between in-duct and far-field angles. At angles greater than the critical angle the transfer function is relatively insensitive to the chosen mode amplitude distribution varying by $\approx \pm 5$ dB for angles up to 65°. At higher angles the sensitivity of the beamformer output to changes in the mode amplitude distribution causes the transfer function to become dependent on the mode model. This limitation cannot be avoided without *a priori* knowledge of the noise sources.

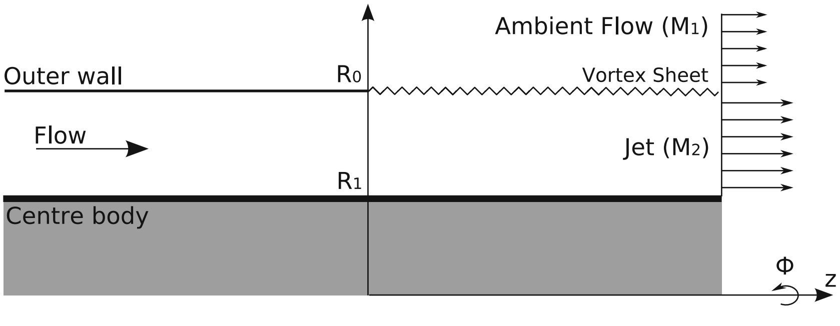

Fig. 8. A schematic of the annular duct geometry used in the simulations of noise radiated from an aeroengine exhaust.

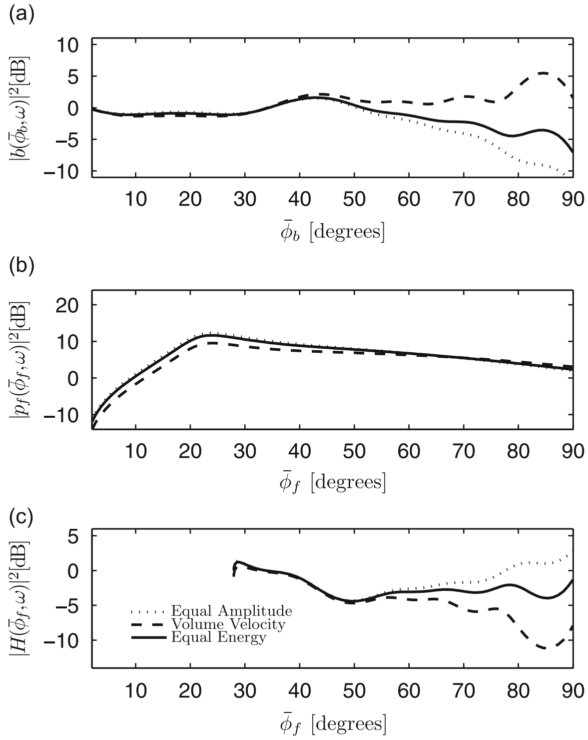

Fig. 9. Beamformer output (a), far-field radiation (b), both plotted in dB with reference to arbitrary pressure, and transfer function (c) for the exhaust configuration. Three different mode-models are shown, the frequency of calculation is $ka=20$.

It should be noted, however, that the mode distribution functions used in this study vary considerably close to cut-off, and as such the differences in predictions at high-angles can be seen as a "worst-case" performance.

Application of this technique in practice will also involve dealing with the challenging issues of using wall-flush mounted microphones in a duct with flow. Principal among these are the contamination of the microphone signals by flow noise and the presence of non-uniform radial flow profiles causing refraction of the mode rays close to the duct wall.

The use of a beamformer is beneficial to the suppression of boundary layer flow noise since delay and sum and delay beamforming essentially enhances the coherent part of the signal, i.e., the acoustic noise, and partially rejects the incoherent, non-acoustic part of the signal. The level of noise rejection is quantified by the array gain. In this way the signal to noise ratio is improved in a manner similar to the 'three-microphone' technique often employed for in-duct measurements [18,12].

Refraction of sound by the boundary layer along the wall in which the microphones are situated may be included in the computation of the transfer function between the beamformer and far field pressure, as given by Eq. (1), for example, ray-tracing techniques or from the modal solution obtained by solving the Pridmore–Brown equation for sheared flows. The significance of these effects on wall-mounted pressure measurements in general remains to be determined. However, there is copious evidence to suggest that in other in-duct measurement approaches, such as modal analysis, results in which the flow is assumed to be uniform, that is with no boundary layer included, are still useful and compare well with theoretical predictions. Tapken et al. [12,13] discuss these issues in more detail.

5. Experimental validation of the no-flow technique

This section presents an experimental verification of the in-duct to far-field measurement technique developed in Section 2. The main aim of the experiment was to verify the estimation of far-field directivity using an in-duct axial microphone array.

5.1. Method

Fig. 10 is a schematic of the experimental set-up. The experiment was performed in the large anechoic chamber and adjoining reverberation chamber at the ISVR. A 4.8 m hard-walled, steel duct of internal diameter 0.4 m was passed through the wall separating the anechoic and reverberation chambers. A thick panel was constructed to hold the duct and ensure good acoustic isolation of the two chambers.

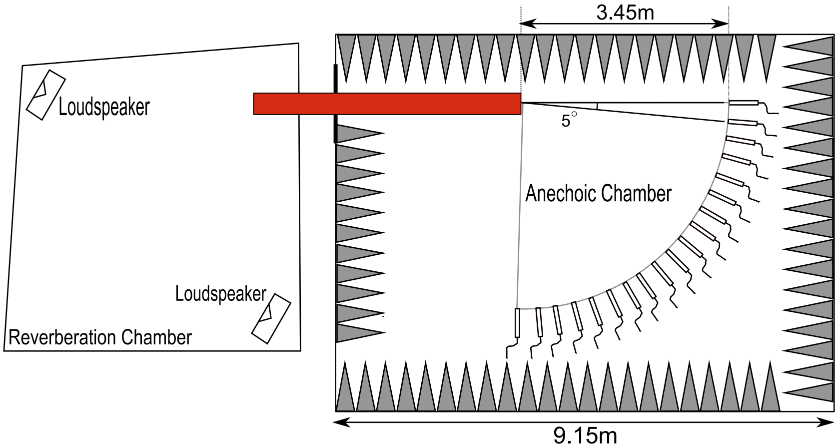

Fig. 10. A plan-view schematic of the experimental set-up. The reverberation chamber is connected to the anechoic chamber by a 4.8 m steel duct. Noise is generated either by two loudspeakers in the reverberation chamber. In the anechoic chamber, the 19 far-field microphone positions trace a circular arc of radius 3.45 m, spaced 5° apart, from 0° (on axis) to 90°.

Fig. 11. A photograph of the in-duct microphone array. Fifteen 7 mm electret microphones were mounted on a thin 50 mm by 400 mm aluminium plate. The microphones were positioned at the edge of the plate, with the centre of the capsules 25 mm apart.

A broadband noise field was created in the duct using a pair of loudspeakers located in the reverberation room, Both the in-duct acoustic pressure and the far-field acoustic pressure were measured simultaneously. The in-duct acoustic pressure was measured using an axial array of 15 microphones mounted at the duct wall. The far-field pressure was measured using a far-field microphone array.

5.1.1. *Reverberation chamber*

Broadband noise was generated in the duct using two Electro-voice 400 W loudspeakers driven by mutually incoherent white noise signals via two power-amplifiers. The white noise signals were pre-generated, pseudo-random sequences produced using MATLAB and stored onto 2 channels of a 24 channel Alesis-ADAT hard-disk recorder.

The reverberation room has non-parallel, highly reflective walls and a volume of 131 m^3. This ensures that the sound field in the room, and hence the sound-field incident on the open end of the duct, is reasonably diffuse. Joseph et al. [8] have shown that this form of excitation creates an *equal energy per mode* sound-field inside the duct, and ensures that all propagating modes are mutually incoherent. Incoherent modes is one of the main assumptions in the in-duct to far-field technique.

5.1.2. *In-duct measurements*

Fig. 11 is a photograph of the in-duct microphone array. Fifteen 7 mm electret microphones were mounted on a thin plate of size 50 mm by 400 mm.

The microphones were positioned at the edge of the plate, with the centre of the microphone capsules separated 25 mm apart. This spacing corresponds to $\lambda/2$ at ka=25 (assuming a sound speed of 340 m s^{-1}), and is the maximum frequency at which the array can be used before aliasing occurs. The microphone spacing is chosen to be as close to $\lambda/2$ at the highest frequency of interest, since this spacing gives an optimal beamformer performance [26]. At lower frequencies something close to this optimal spacing can be maintained by using only, for example, every other microphone in the array. Here, however, we use all microphones at all frequencies.

The microphone cables passed through small holes in the plate, and were affixed to the underside of the plate so as to minimise their effect on the sound field in the duct.

The microphone array was located along the bottom of the duct, and as close as possible to the duct wall (Fig. 12). The first microphone in the array was positioned 1.2 m from the open end of the duct, so as to minimise the effect of reflections from the open end.

Each microphone was connected to a custom-made signal amplifier. The time series were sampled simultaneously using a 32 channel SONY DAT recorder at a sampling rate of 48 kHz with 16 bit resolution. The total recording time for each test was 1 min.

The array data were post-processed to create a cross-spectral matrix at each discrete frequency point using the MATLAB Signal Processing Toolbox functions `cpsd` and `pwelch`. A Welch spectral estimation algorithm was used (2048 point FFT, Hamming window and 50 percent overlap).

To account for the differences in magnitude and phase of the individual array microphones, calibration was performed by multiplying the complex pressure spectrum of the i th microphone $p_i(\omega)$ by a transfer function, $G_{iR}(\omega)$. The transfer function $G_{iR}(\omega)$ is the transfer function between the i th array microphone and a reference microphone averaged over four loudspeaker positions. This transfer function was measured in an anechoic chamber by placing a B&K type 4185 microphone 5 mm away from the diaphragm of each of the array microphones in turn. White noise was generated with a loudspeaker, and the transfer function between the two microphones was measured.

The cross-spectral matrix, $\mathbf{S}_{pp}$, in each frequency bin was formed from

$$\mathbf{S}_{pp} = \begin{bmatrix} |G_{1R}|^2 S_{p_1p_1} & G_{1R}S_{p_1p_2}G_{2R}^* & \cdots & G_{1R}S_{p_1p_N}G_{NR}^* \\ G_{2R}S_{p_2p_1}G_{1R}^* & |G_{2R}|^2 S_{p_2p_2} & & \\ \vdots & \vdots & \ddots & \\ G_{NR}S_{p_Np_1} & & & |G_{NR}|^2 S_{p_Np_N} \end{bmatrix} \tag{41}$$

where $S_{p_ip_j} = E\{(\pi/T)p_i(\omega)p_j^*(\omega)\}$ is the pressure cross spectral density between microphone i and microphone j.

Following the theory presented in Section 2.3 the beamformer output corresponding to a beamsteer angle ϕ is

$$S_{bb}(\phi,\omega) = \frac{1}{N^2}\mathbf{w}(\phi,\omega)\mathbf{S}_{pp}\mathbf{w}^H(\phi,\omega) \tag{42}$$

where $\mathbf{w}$ is the vector of weight coefficients, calculated from Eq. (10). Note Eq. (42) is simply a restatement of Eq. (9) in matrix form, with the measured cross-spectral matrix replacing the predicted pressures of Eq. (9).

5.1.3. Far-field measurements

Measurements of the far-field directivity were made in the anechoic chamber. The size of the chamber, not including wedges, is 7.33 m × 7.33 m × 5.50 m. The cut-off frequency of the wedges is 80 Hz. The mesh floor of the chamber was

Fig. 12. A photograph of the microphone array positioned in the duct. The microphones themselves lay on an axial line, and are as close as possible to the duct wall.

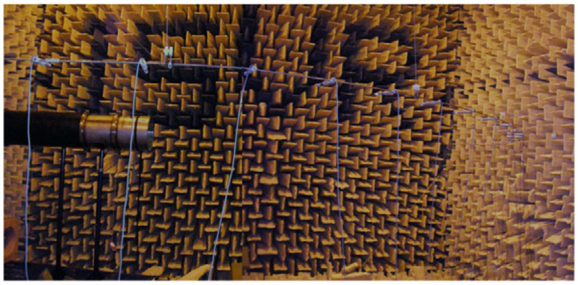

Fig. 13. A photograph of the anechoic chamber taken from the main entrance. The far-field microphone array consists of 19 microphones suspended from the ceiling in a polar arc. The chamber floor has been removed to minimise reflections, except for a small area directly underneath the duct to allow access for the in-duct measurements. The duct is connected to the reverberation chamber through a baffled panel.

removed to minimise reflections. Fig. 13 is a photograph of the anechoic chamber taken from the main entrance showing the duct and the far-field array.

Far-field measurements were made at 19 positions spanning a 90° arc of 3.45 m radius, whose centre was located at the centre of the duct exit. The far-field microphone array was positioned at the same height as the centre of the duct exit, defined as an azimuthal angle of 0°. The microphones were positioned at 5° increments from 0° (on axis) to 90° (sideline) as shown in Fig. 10. The radiated sound field was assumed to be axi-symmetric consistent with the assumption of incoherent modes. Therefore the radiation is independent of azimuthal angle.

Far-field measurements were made using B&K type 4185 condenser microphones, connected to custom-made amplifiers. The same acquisition and post-processing hardware was used for both the in-duct and far-field microphones.

Noise-floor measurements were made both in-duct and in the far-field. Signal to noise ratio in the frequency range of interest, $ka < 30$, in the far-field was greater than 50 dB on axis falling to approximately 30 dB at 90°. The in-duct signal to noise ratio was greater than 55 dB.

5.2. Results

In this section the far-field polar directivity, calculated by multiplying the beamformer response by the predicted transfer function $|H(\phi_f,\omega)|^2$, is compared to the directly measured far-field directivity. Predicted far-field directivities are obtained using the full transfer function, $|H(\phi_f,\omega)|^2$, given by Eq. (16) and based on a flanged duct model.

Far-field directivity predictions are presented in 1/3 octave frequency bands. The predicted far-field squared pressure in a given third-octave band with centre frequency ω_c is the sum of the narrow band predicted directivities at frequencies between ω_l and ω_u,

$$|p_f(\phi,\omega_c)|^2 = \sum_{\omega_i=\omega_l}^{\min\{\omega_u,\omega_{\max}\}} |H(\phi,\omega_i)|^2 |b(\phi,\omega_i)|^2 \Delta\omega_i \tag{43}$$

where $\Delta\omega_i$ is the analysis frequency bandwidth, and $\omega_{\max}$ is the frequency at which the in-duct array is aliased.

In the plots that follow the solid curves correspond to the predicted far-field directivity obtained using $|H(\phi_f,\omega)|^2$ calculated from Eq. (16). The crosses are the measured far-field directivities. The lower plots in each figure are the normalised beamformer outputs, $|b(\phi_b,\omega)|^2$, as a function of beamsteer angle. Solid horizontal lines in the lower plots show the beamwidth of the in-duct beamformer at 45°.

Fig. 14 shows the results for the 4000 Hz third-octave band, corresponding to ka=14.8 (lower frequency ka=13, upper frequency ka=16.4). The shape of the predicted directivity is in good agreement with that measured from 10° to approximately 70°. At high angles the flanged duct model used in the prediction of $|H(\phi_f,\omega)|^2$ is the most probable cause of the discrepancies at high angles, and a model more appropriate to the unflanged duct used would improve the predictions.

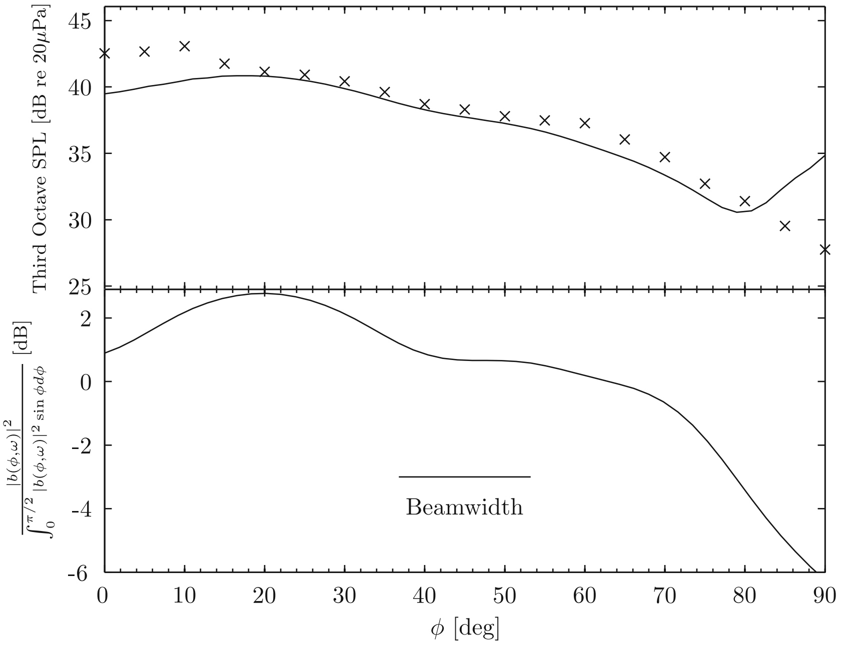

Fig. 14. Predicted far-field directivities (top) and normalised beamformer output (bottom) in the 4000 Hz (ka=14.6) third-octave band using an array of 15 microphones spaced 2.5 cm apart. The solid curve in the top plot uses the full transfer function and the crosses denote measured far-field pressures.

The overall level in the far-field is well-predicted to within 1 dB up to 70°. At low angles the technique under-predicts the far-field levels, this is likely due to a combination of the duct having greater on-axis directivity when fewer modes are able to propagate, and the low-angle beamformer correction presented in Eq. (22) not performing well at low-frequencies.

The normalised beamformer output in Fig. 14 has a magnitude variation of approximately 2 dB over the range of angles $0^\circ \le \phi \le 75^\circ$. This variation is larger than that predicted for the equal energy per mode model in Section 3.2 but not as large as for the equal amplitude or the volume velocity source model.

Fig. 15 shows the results for the 5000 Hz third-octave band, corresponding to $ka = 18.4$ (lower frequency $ka = 16.4$, upper frequency $ka = 20.6$). The difference between the predicted and measured far-field levels is now smaller at lower angles. The measured directivity levels are well predicted to within 2 dB between 10° and 70°.

Fig. 16 shows the results for the 6300 Hz third octave band, corresponding to $ka = 23.1$ (lower frequency $ka = 20.6$, upper frequency $ka = 25$). This is the highest frequency band investigated, as frequencies above 6800 Hz ($ka = 25$) are aliased by the in-duct array. The predicted directivity levels are less than 1 dB away from the measured directivity from 0° to 70°. The predicted directivity pattern follows the measured pattern very closely.

The variation in level of the normalised beamformer output in this frequency band is also much smaller, indicating that the sound field has approximately equal energy per mode.

6. Conclusion

A far-field directivity prediction technique has been proposed that uses an in-duct axial array of microphones to predict the sound field radiated from the open end of the duct, assuming that the in-duct sound field consists of incoherent modes. We have shown that the transfer function used to relate the in-duct beamformer output to the corresponding radiated far-field directivity pattern is very nearly independent of the mode amplitude distribution in the duct for a large range of in-duct angles less than 80°. A limitation of the technique is that at higher angles the prediction becomes sensitive to the chosen mode amplitude distribution due to the small number of modes propagating at these high angles.

The transfer function for a no-flow duct has been fully investigated, and a numerical transfer function approach for aeroengine exhaust ducts has been proposed.

The principle advantage of this technique, over, for example determining the mode amplitudes by modal decomposition and using these as the input to a radiation model, is the relatively small number of microphones required. An array of around 15 microphones spaced half a wavelength apart has been shown to be sufficient to predict the far-field directivity pattern. This performance has been demonstrated using a no-flow laboratory scale rig. In practice, the transfer functions required can easily be calculated in advance of a measurement campaign. This allows rapid prediction of the far-field directivity, and enables engineers to quickly asses the effect of build changes on the radiated sound.

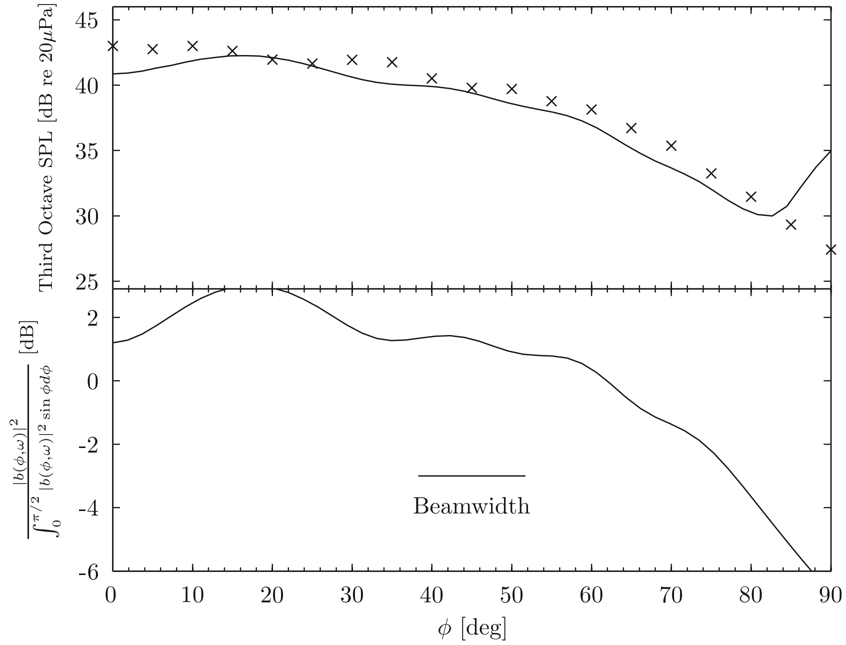

Fig. 15. Predicted far-field directivities (top) and normalised beamformer output (bottom) in the 5000 Hz ($ka = 18.4$) third-octave band using an array of 15 microphones spaced 2.5 cm apart. The solid curve in the top plot uses the full transfer function and the crosses denote measured far-field pressures.

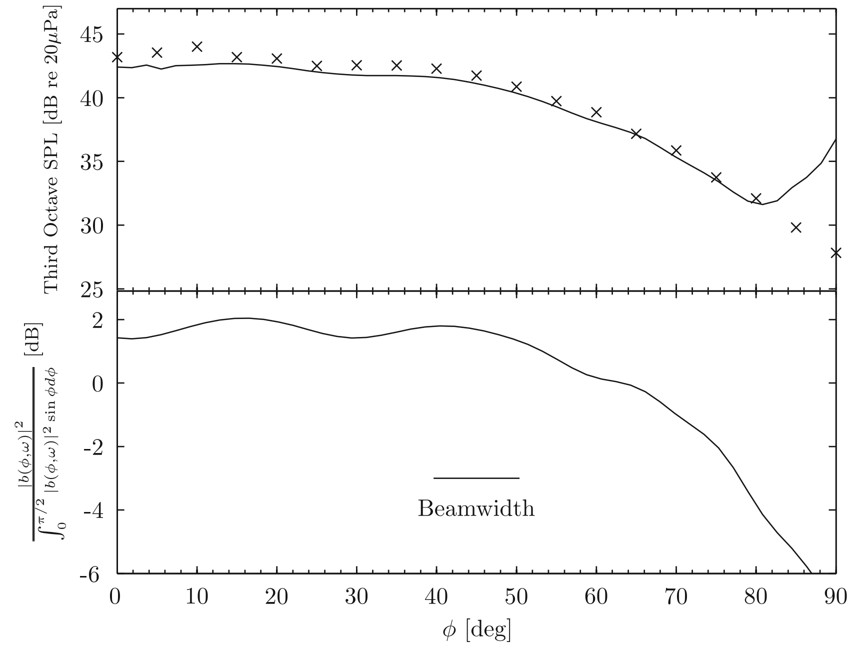

Fig. 16. Predicted far-field directivities (top) and normalised beamformer output (bottom) in the 6300 Hz (ka=23.15) third-octave band using an array of 15 microphones spaced 2.5 cm apart. The solid curve in the top plot uses the full transfer function and the crosses denote measured far-field pressures.

Acknowledgments

The authors Lowis and Joseph graciously acknowledge the financial support of Rolls-Royce plc through the ISVR University Technology Centre.

Appendix A. The equivalence of an equal energy per mode sound field and isotropic noise

Here we show that an equal energy per mode sound field in a duct in the high-ka limit is equivalent to a semi-isotropic noise field. Assuming incoherent modes the total squared pressure at the duct wall, $|p_w(\omega)|^2$, can be written as the sum of the squared modal pressure due to each mode,

$$|p_w(\omega)|^2 = \sum_{mn} |p_w(\phi_{mn},\omega)|^2 \tag{44}$$

In the high-ka limit the summation in Eq. (44) can be written as an integral over in-duct angle ϕ,

$$|p_w(\omega)|^2 = \int_0^{\pi/2} |p_w(\phi,\omega)|^2 \, d\phi \tag{45}$$

where $|p_w(\phi,\omega)|^2$ is integrated over the *continuous* mean square pressure per unit angle ϕ. By taking the integral from 0 to $\pi/2$ we are assuming sound propagation in one direction only.

From Eq. (18) the squared model amplitude in an equal energy per mode sound field, with M=0, varies as $|A(\phi_{mn})|^2 \propto 1/\cos(\phi_{mn})$. Therefore $|p_w(\phi,\omega)|^2$ can be written as

$$|p_w(\phi,\omega)|^2 \propto \frac{n(\phi)}{\cos\phi \langle \Lambda \rangle} \tag{46}$$

where $\langle \Lambda \rangle$ is the mode-normalisation constant averaged over m and n, introduced to correct for the fact that measurements are made at the duct wall. Joseph et al. show that $\langle \Lambda \rangle \to 2$ as $ka \to \infty$. From Rice [20], $n(\phi)$ may be written as

$$n(\phi) = 2\sin\phi\cos\phi \tag{47}$$

Combining Eqs. (46) and (47) the mean square pressure in a small bandwidth dϕ is

$$|p_w(\phi,\omega)|^2 \, \mathrm{d}\phi \propto \sin\phi \, \mathrm{d}\phi \tag{48}$$

In Eq. (48) $\sin\phi \, \mathrm{d}\phi$ is also proportional to the elementary solid angle since $d\Omega = 2\pi\sin\phi \, \mathrm{d}\phi$. Thus $d|p_w|^2/d\Omega$ is constant and an equal energy per mode sound field tends to a diffuse field.

References

[1] U. Bolleter, M. Crocker, Theory and measurement of modal spectra in hard-walled cylindrical ducts, *Journal of the Acoustical Society of America* 51 (1972) 1439–1447.

[2] U.W. Ganz, P.D. Joppa, T.J. Patten, D.F. Scharpf, Boeing 18-inch fan rig broadband noise test, Technical Report CR-1998-208704, NASA, 1998.

[3] L. Enghardt, C. Lowis, L. Neuhaus, Broadband sound power determination in flow ducts, *10th AIAA/CEAS Aeroacoustics Conference*, Manchester, UK, 2004.

[4] L. Enghardt, A. Holewa, U. Tapken, Comparison of different analysis techniques to decompose a broad-band ducted sound field in its mode constituents, *13th AIAA/CEAS Aeroacoustics Conference*, Rome, 2007, AIAA-2007-3520.

[5] P. Sijtsma, Feasibility of in-duct beamforming, *13th AIAA/CEAS Aeroacoustics Conference*, Rome, 2007, AIAA-2007-3696.

[6] E. Rice, M. Heidmann, Modal propagation angles in a cylindrical duct with flow and their relation to sound radiation, *17th Aerospace Sciences Meeting*, New Orleans, 1979.

[7] C. Chapman, Sound radiation from a cylindrical duct. Part 2. Source modelling, nil-shielding directions, and the open-to-ducted transfer function, *Journal of Fluid Mechanics* 313 (1996) 367–380.

[8] P. Joseph, C. Morfey, C. Lowis, Multi-mode sound transmission in ducts with flow, *Journal of Sound and Vibration* 264 (2003) 523–544.

[9] T.F. Brooks, W.M. Humphreys, A deconvolution approach for the mapping of acoustic sources determined from phased microphone arrays, *Journal of Sound and Vibration* 294 (2006) 856–879.

[10] C. Lowis, P. Joseph, A. Kempton, An in-duct beamformer for the estimation of far-field directivity, *14th AIAA/CEAS Aeroacoustics Conference*, Vancouver, BC, Canada, 2008.

[11] R.P. Dougherty, J.M. Mendoza, Nacelle in-duct beamforming using modal steering vectors, *14th AIAA/CEAS Aeroacoustics Conference*, Vancouver, BC, Canada, 2008, AIAA-2008-2812.

[12] U. Tapken, R. Bauers, F. Arnold, J. Zillmann, Turbomachinery exhaust noise radiation experiments—part 2: in-duct and far-field mode analysis, *14th AIAA/CEAS Aeroacoustics Conference*, Vancouver, BC, Canada, 2008.

[13] U. Tapken, L. Enghardt, Optimisation of sensor arrays for radial mode analysis in flow ducts, *12th AIAA/CEAS Aeroacoustics Conference*, Cambridge, MA, USA, 2006, AIAA 2006-2638.

[14] C.R. Lowis, P. Joseph, A focused beamformer technique for separating rotor and stator-based broadband sources, *12th AIAA/CEAS Aeroacoustics Conference*, Cambridge, MA, USA, 2006, AIAA 2006-2520.

[15] J. Premo, P. Joppa, Fan noise source diagnostic test—wall measured circumferential array mode results, *8th AIAA/CEAS Aeroacoustics Conference*, Brekenridge, CO, USA, 2002, AIAA 2002-2429.

[16] C.R. Lowis, In-duct measurement techniques for the characterisation of broadband aeroengine noise, PhD thesis, University of Southampton, UK, 2007.

[17] P. Joseph, C.L. Morfey, Multimode radiation from an unflanged, semi-infinite circular duct, *Journal of the Acoustical Society of America* 105 (1999) 2590.

[18] J.Y. Chung, The rejection of flow noise using a coherent function method, *Journal of the Acoustical Society of America* 62 (1977) 388–395.

[19] F. Castres, P. Joseph, Experimental investigation of an inversion technique for the determination of broadband duct mode amplitudes by the use of near-field sensor arrays, *Journal of the Acoustical Society of America* 122 (2007) 848–859.

[20] E. Rice, Modal density function and number of propagating modes in ducts, Technical Memorandum TM X-73539, NASA, 1976, Presented at the 92nd Meeting of the Acoustical Society of America, San Diego, CA, November 16–19, 1976.

[21] W.S. Burdic, *Underwater Acoustic Signal Analysis*, Prentice-Hall, Upper Saddle River, New Jersey, USA, 1984.

[22] G. Gabard, R.J. Astley, Theoretical model for sound radiation from annular jet pipes: far- and near-field solutions, *Journal of Fluid Mechanics* 549 (2006) 315–341.

[23] R. Munt, Acoustic radiation from a circular cylinder in a subsonic stream, *Journal of the Institute of Mathematics and its Applications* 16 (1975) 1–10.

[24] R. Sugimoto, R. Astley, L. De Mercato, K. Holland, V. Jurdic, Prediction methods for propagation in bypass ducts and comparison with measured data, *11th AIAA/CEAS Aeroacoustics Conference*, Monterey, CA, 2005, AIAA-2005-3059.

[25] M. Goldstein, *Aeroacoustics*, McGraw-Hill, New York, 1976.

[26] D.H. Johnson, D.E. Dudgeon, *Array Signal Processing: Concepts and Techniques*, Prentice-Hall, Upper Saddle River, New Jersey, USA, 1993.